I&EC research
Industrial & Engineering Chemistry Research

A novel fused metal anode solid electrolyte fuel cell for direct coal gasification: a steady-state model

Ioannis V. Yentekakis, Pablo G. Debenedetti, and Bruno Costa

Ind. Eng. Chem. Res., **1989**, 28 (9), 1414-1424 • DOI: 10.1021/ie00093a022

Prasada Rao, T. S. R. *Advances in Catalysis Science and Technology*; Wiley Eastern Ltd.; New Delhi, India, 1985.
Rollmann, L. D. Inorganic Compounds with Unusual Properties. *Adv. Chem. Ser.* **1979**, *No. 173*.
Whyte, T. E., Jr.; Dalla Betta, R. A. Zeolite Advances in the Chemical and Fuel Industries: A Technical Perspective. *Catal. Rev. Sci. Eng.* **1982**, *24*, 567.

Received for review February 6, 1989
Accepted May 2, 1989

A Novel Fused Metal Anode Solid Electrolyte Fuel Cell for Direct Coal Gasification: A Steady-State Model

Ioannis V. Yentekakis and Pablo G. Debenedetti*
Department of Chemical Engineering, Princeton University, Princeton, New Jersey 08544-5263

Bruno Costa
80122 Naples, Italy

The simultaneous gasification of coal and the generation of electrical current in a high-temperature solid electrolyte fuel cell of the form C, O_2, fused metal/ZrO_2 (8 mol % Y_2O_3)/Pt, O_2 with a fused metal anode is a promising new concept. This process utilizes part of the Gibbs energy change of the coal gasification reaction to generate electricity with the high thermodynamic efficiency characteristic of fuel cells. We present a lumped parameter model that describes the steady-state behavior of this novel fuel cell and discuss the effect of operating conditions upon cell performance. The electrochemical cell reactor is capable of producing very high current and power densities and exhibits steady-state multiplicity over a wide range of operating conditions.

In the last 10 years, there has been an increased interest in the utilization of solid electrolytes in heterogeneous catalysis (Vayenas, 1988). Zirconia-based solid electrolyte cells, for example, have found extended use in the investigation of the kinetics of heterogeneous oxidation reactions (Wagner, 1970; Vayenas et al., 1980; Stoukides and Vayenas, 1982a, 1983; Yentekakis et al., 1988; Metcalfe and Sundaresan, 1988) and, more recently, in the electrochemical modification of the catalytic activity of metals (Yentekakis and Vayenas, 1988; Vayenas, 1988; Vayenas et al., 1988; Bebelis and Vayenas, 1989; Neophytides and Vayenas, 1989). The latter application, in particular, has obvious technological significance and promises further use of these materials in heterogeneous catalytic processes.

Yet another important application of solid electrolyte devices is their use in high-temperature fuel cells for the simultaneous production of chemicals and electricity. This mode of operation combines the concepts of a fuel cell and of a chemical reactor. Fuel cells can convert a significant portion of the Gibbs energy change of exothermic reactions into electricity rather than heat, their thermodynamic efficiency comparing favorably (Bockris and Reddy, 1970) with cyclic thermal power generation schemes which are limited by Carnot-type constraints. Another advantage of these devices is that they allow operation at temperatures of catalytic interest where activation polarization phenomena usually diminish or vanish.

The operation of such zirconia-based solid electrolyte fuel cells has been investigated experimentally, up to the pilot plant scale (Weissbart and Ruka, 1962; Etsell and Flengas, 1971; Farr and Vayenas, 1980; Vayenas and Farr, 1980; Sigal and Vayenas, 1981; Stoukides and Vayenas, 1982b; Michaels and Vayenas, 1984a,b; Michaels et al., 1986; Manton, 1986; Kiratzis and Stoukides, 1987; Yentekakis and Vayenas, 1989) as well as theoretically (Debenedetti and Vayenas, 1983; Vayenas et al., 1985). A number of industrially important oxidations, such as the conversion of ammonia to nitric oxide (Vayenas and Farr, 1980; Sigal and Vayenas, 1981; Farr and Vayenas, 1980), the Andrussov process for the production of HCN (Kiratzis and Stoukides, 1987), the oxidative dehydrogenation of ethylbenzene to styrene (Michaels and Vayenas, 1984a,b) and 1-butene to butadiene (Manton, 1986), the direct oxidation of H_2S to SO_2 (Yentekakis and Vayenas, 1989), and the ethylene epoxidation (Stoukides and Vayenas, 1982b), have been carried out in experimental cells. Solid electrolyte fuel cells, operating on H_2 or CO as the fuel, have been constructed and tested for years (Weissbart and Ruka, 1962; Archer et al., 1965; Etsell and Flengas, 1971; Michaels et al., 1986). Comprehensive reviews of solid oxide fuel cells (Brown, 1986; Vayenas, 1988) and of the use of the fuel cells in electric utility power generation (Frickett, 1986) have appeared recently in the literature.

The purpose of this paper is to present a new concept for the industrially important coal gasification process based on the use of solid electrolyte devices. This process allows, in principle, the clean, efficient cogeneration of carbon monoxide and electric power. The fuel cell modeled here is quite different from those previously described in the literature (Debenedetti and Vayenas, 1983) because it includes a fused metal bulk anode, instead of thin metallic catalyst films.

The Process

Coal gasification in molten metal baths is a relatively new process. Considerable effort, mostly in Japan (Nakajima et al., 1983), has been devoted to the investigation of the scientific and economic implications of this technology. Important technological advantages of this process include the ability to produce low-sulfur coal gas (consisting mainly of CO and H_2) continuously and with high gasification efficiency and the potential for combining gasification with steel making through the use of excess gasification heat for ore smelting or scrap remelting. The economics of fused iron bath gasification can be made even more attractive if part of the Gibbs energy change of the

* To whom all correspondence should be addressed.

0888-5885/89/2628-1414$01.50/0

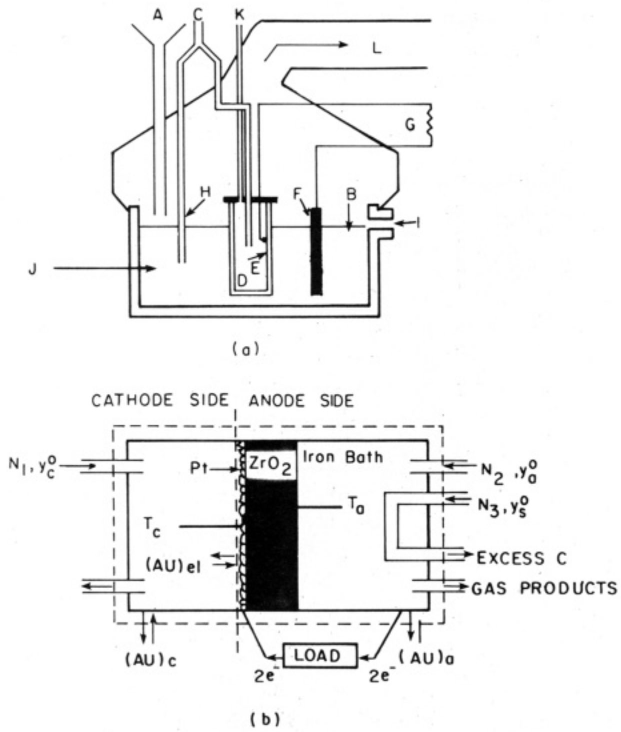

Figure 1. Schematic representation of the fused bath process (a) and of control volumes for macroscopic balance equations (b).

oxidation reaction is directly converted into electricity through the use of oxygen-anion-conducting solid electrolytes such as yttria-stabilized zirconia (Subbarao and Maiti, 1984). This combination of fuel cell and fused metal gasifier in a single reactor is the distinguishing feature of the new process described here (Costa, 1987).

The idea of combining coal gasification and fuel cells is not a new one. Previous efforts, however, have been aimed at developing a process in which the fuel produced in a gasifier is burnt in a physically separate fuel cell, generating electricity with high thermodynamic efficiency (Appleby, 1987). Recently, Nakagawa and Ishida (1988) have reported on the performance of an experimental fuel cell in which charcoal is directly gasified at the anode. In the new process described here, on the other hand, the gasification occurs in a molten metal anode. This has the important advantage of lowering significantly the presence of gas-phase SO_x and NO_x (Nakajima et al., 1983).

Figure 1a is a schematic representation of the fused bath process. Finely divided carbon (A) is fed pneumatically to the fused iron anode (B) by means of nitrogen or a similar inert carrier. Air (C) is fed into the cell's cathodic compartment (D), made of yttria-stabilized zirconia or a similar oxygen-anion-conducting solid electrolyte. The inner (cathodic) walls of the solid electrolyte are coated with porous Pt (Farr and Vayenas, 1980; Michaels et al., 1986) or an equivalent film (E) having high catalytic activity for the dissociation of oxygen molecules. Upon diffusion into the film's pores, oxygen is ionized according to the cathodic half-reaction

$$\tfrac{1}{2}O_2(g) + 2e^- \rightarrow O^{2-} \tag{1}$$

which occurs at the three-phase boundary between air, Pt, and zirconia. Anions migrate across the solid electrolyte's wall. At the molten iron–zirconia interface, the anodic half-reaction occurs,

$$O^{2-} \rightarrow 2e^- + \underline{O} \tag{2}$$

where the underbar denotes atomic oxygen [dissolved oxygen in carbon-containing liquid Fe exists only in this form (Rao, 1985; Coudurier et al., 1985)]. The electrical circuit, in which F is the anodic current collector, is closed by an external load (G). Note that the resistivity of molten Fe is extremely low (ca. 1.55×10^{-6} Ω·m at 1500 °C for iron with 3.8% C), comparing favorably even with recently developed perovskite-type porous electrodes (Brown, 1986). The net result of the transport of oxygen from cathode to anode is thus electric power.

Atomic oxygen then reacts with dissolved carbon ($\underline{C}$) throughout the liquid anode,

$$\underline{C}\ (\text{in Fe}) + \underline{O} \rightarrow CO(g) \tag{3}$$

The overall process, therefore, allows coal to be gasified with simultaneous cogeneration of electric power.

Coal gasification in molten metal baths occurs via the homogeneous oxidation of dissolved carbon with atomic oxygen (Solar and Guthrie, 1972), as described by eq 3. In the present, electrochemical case, however, there is the additional possibility of oxidizing the carbon directly with oxygen anion,

$$O^{2-} + \underline{C} \rightarrow CO(g) + 2e^- \tag{3a}$$

Thermodynamically, both pathways are indistinguishable, as shown in the Appendix section. Nevertheless, eq 3a is a heterogeneous reaction occurring at the molten iron–zirconia interface. It is not possible to predict a priori whether the common homogeneous reaction (eq 3) or its hypothetical heterogeneous counterpart (eq 3a) will occur in an actual fused bath cell. The present lumped model therefore describes a cell in which the homogeneous reaction takes place, as is known to be the case in molten metal gasifiers.

Oxygen can also be fed directly into the anode (H) to provide part of the heat of reaction needed in order to sustain steady operation at high temperatures. This mode of operation implies, in principle, a compromise between a higher rate of heat generation and a lower thermodynamic driving force for the transfer of oxygen across the solid electrolyte. Actual calculations, however (see Results and Discussion section), show a negligible effect upon cell voltage and a significant enhancement of heat generation. Nitrogen-rich and carbon monoxide rich gas streams are produced at the cathode (K) and anode (L), respectively.

Figure 1a also includes an overflow (I) through which sulfur-rich, insoluble impurities or excess carbon are continously removed, as well as a make-up molten iron stream (J) introduced via a magnetic pump. Practical configurations currently under investigation include separate reactors for carbon dissolution (carburization), sulfur removal (desulfurization), and partial oxidation of the carbon dissolved in the molten iron by noncathodic oxygen (Costa, 1988). Figure 1a is therefore indicative of the fused bath fuel cell process and not of a specific reactor configuration.

In this paper, we derive the macroscopic balance equations for the fuel cell reactor shown schematically in Figure 1a. We consider well-mixed anodic and cathodic compartments and batch operation with respect to the iron. This model is of considerable importance since any real reactor that deviates from the assumed perfect mixing can always be described mathematically through the electrical and/or hydraulic superposition, in series or in parallel, of elementary units such as the one we describe here (Debenedetti and Vayenas 1983).

Governing Equations

Thermodynamic and Kinetic Constraints. In order to analyze the well-mixed cell's performance, we must write macroscopic balances of mass and energy. These will then be solved simultaneously with the electrical equations. In this work, the solution of the governing equations is based on the assumption of carbon saturation at the anode (see Appendix section), which implies negligible iron oxidation (Nomura and Mori, 1973; Rao, 1985). At the temperatures of interest for molten Fe operation, carbon dioxide production can be neglected (Gaskell, 1981). In addition, the liquid-phase reaction between atomic oxygen and dissolved carbon is taken to be the rate-determining step of the overall anodic process.

Operation at relatively high dissolved carbon levels is advantageous from two different points of view. Firstly, the rate of the gasification reaction (and hence the power density) will increase with high carbon content in the anode. Secondly, the bath's melting point can be significantly lowered by the presence of dissolved carbon: the Fe–C system has a eutectic point at 1153 °C and 4.26% wt C (Chipman, 1972), that is to say 380 °C lower than the melting point of pure Fe.

For the elementary reaction between dissolved atomic oxygen and dissolved carbon, we can write a general second-order mass action expression (see Appendix section)

$$r = k_r[\%\mathrm{C}]\{[\%\underline{\mathrm{O}}] - y_{\mathrm{CO}}/K_e\}\phi_1\phi_2 \qquad (4)$$

where

$$\phi_1 = \frac{\rho_{\mathrm{Fe}}}{1600} \qquad \phi_2 = \frac{\rho_{\mathrm{Fe}}}{12(100 - [\%\underline{\mathrm{C}}])}$$

Equation 4 requires clarification. Mass-transfer limitations are excluded by hypothesis in a well-mixed reactor, such as the one we are considering here (i.e., well-mixed anode and cathode). The reaction, furthermore, occurs in the liquid phase, between dissolved carbon and dissolved atomic oxygen. This is fundamentally different from all previous decarburization processes, in which the reaction is heterogeneous, involving either a jet of C-containing molten iron being exposed to air (Baker and Ward, 1967) or the bubbling of oxygen–inert gas or CO_2–CO mixtures in the molten bath (Nomura and Mori, 1973; Sain and Belton, 1976; Suzuki and Mori, 1977). These heterogeneous processes have invariably been found to be mass transfer limited.

Because of the novelty of the concept discussed here, there is yet no information in the literature on the kinetics of the homogeneous, liquid-phase reaction between dissolved carbon and atomic oxygen. We have therefore used k_r as a parameter: with typical values for liquid-phase second-order frequency factors and activation energies as a base case, these quantities were systematically varied in such a way as to explore the effect of changes in k_r, spanning several orders of magnitude, upon reactor performance. Gas-phase anodic oxygen (H, Figure 1a) is always assumed to be in equilibrium with dissolved atomic oxygen (see Appendix section).

Macroscopic Balance Equations. We now discuss the macroscopic balances of mass and energy which, when solved simultaneously with Khirchoff's and Nernst's equations, yield the steady state(s) corresponding to a given set of inlet and boundary conditions (we use the latter term in a thermodynamic, rather than mathematical, sense). To this end, we consider Figure 1b. We first write a steady-state oxygen balance for the cathode,

$$N_1 y_c^0 x_c = \frac{I}{4F} \qquad (5)$$

where N_1 is the total cathodic molar feed rate (with an oxygen mole fraction y_c^0), x_c is the cathodic conversion of oxygen, I is the current, and F is Faraday's constant. Similarly, the corresponding anodic oxygen balance reads

$$(N_1 y_c^0 x_c + N_2 y_a^0) x_a = \frac{rV_a}{2} \qquad (6)$$

where N_2 is the molar anodic gaseous feed rate (with an oxygen mole fraction y_a^0), x_a is the anodic conversion of oxygen, V_a is the volume of a single fused bath anode, and r is the reaction rate, which is given by eq 4. Note that, contrary to the usual situation encountered in high-temperature fuel cells (Debenedetti andd Vayenas, 1983), anodic oxygen feed introduces the need for a second oxygen material balance (eq 6) in order to account for electrochemical as well as direct (or chemical) oxygen conversion.

There is ample experimental evidence on the nature of voltage losses in high-temperature solid electrolyte cells (Weissbart and Ruka, 1962; Etsell and Flengas, 1971; Farr and Vayenas, 1980; Vayenas and Farr, 1980; Michaels and Vayenas, 1984a,b; Yentekakis and Vayenas, 1989). At the high temperatures of interest here, cathodic and anodic activation overpotentials are usually negligible. Further progress in the reduction of activation overpotentials has been achieved recently through the development of complex oxide electrodes of the perovskite family having high electronic conductivity, thermal and chemical stability, high porosity, and good catalytic activity for oxygen dissociation (Brown, 1986; Takeda et al., 1987; Franke and Winnick, 1988).

Concentration polarization may arise from external (bulk to electrode) or internal mass-transfer limitations. We consider first the former. In a process taking place according to eq 3 (bulk chemical gasification), atomic oxygen transport away from the solid electrolyte is the potential source of concentration polarization; carbon transport to the solid electrolyte is important in the case of direct electrochemical oxidation (eq 3a). For typical industrial molten iron gasifier conditions, mass-transfer coefficients for atomic oxygen and dissolved carbon have been determined by Suzuki and Mori (1977), who give values of $k_0 = 3.5 \times 10^{-4}$ m/s (oxygen) and $k_c = 5.1 \times 10^{-4}$ m/s (carbon) at 1580 °C. Using these coefficients, one can calculate the current density (i) necessary to create a concentration difference between the solid electrolyte–molten iron interface and the bulk solution of the order of the bulk concentration of the species of interest [i.e., $i/4F = k_0\Delta C$ for oxygen and $i/2F = k_c\Delta C$ for carbon, where ΔC (in appropriate units) is ca. 0.1% by weight for oxygen and 3% by weight for carbon]. The calculated values are 3 A/cm^2 (oxygen transport limiting; homogeneous chemical gasification) and 178 A/cm^2 (carbon transport limiting; heterogeneous electrochemical gasification). Thus, for the more stringent case of interest here (oxygen transport limiting), external mass-transfer limitations are unimportant for i lower than ca. 3 A/cm^2.

As for internal mass-transfer limitations, they can be greatly reduced by using highly porous electrodes (Bockris and Reddy, 1970; Teague, 1981; Debenedetti and Vayenas, 1983). Assuming purely ohmic polarization, therefore, we can write

$$E = E_{\mathrm{rev}} - I(R_i + R_{\mathrm{el}}) \qquad (7)$$

with

$$E = IR_{\mathrm{ex}} \qquad (8)$$

where E is the actual cell voltage, E_{rev} is the open-circuit cell voltage, I is the current, R_{ex} is the external load, R_i is the solid electrolyte's ohmic resistance, and R_{el} is the resistance due to the electrodes. The electrolyte's resistance is an exponentially decreasing function of temperature (Archer et al., 1965; Debenedetti and Vayenas, 1983)

$$R_i = 4.17 \times 10^{-5} \exp\left(\frac{9700}{T}\right)\frac{\delta}{A_{el}} \quad (\Omega) \tag{9}$$

The open-circuit voltage is given by (see Appendix section)

$$E_{rev} = \frac{RT}{4F} \ln\left(\frac{p_{O_{2,c}}}{p_{O_{2,a}}}\right) \tag{10}$$

where $p_{O_{2,c}}$ and $p_{O_{2,a}}$ are the partial pressures of oxygen in the well-mixed cathode and in the anodic gas product stream, respectively (the latter being in equilibrium with dissolved atomic oxygen). If the electrode materials on the anode and cathode are different, eq 10 contains an additive correction (the contact potential) that accounts for the difference in chemical potential of electons on different materials. This small correction is normally neglected (Bockris and Reddy, 1970), and we do not include it in what follows. It is worth noting that E_{rev} can also be computed by considering the Gibbs energy change of the reaction

$$C(s) + \tfrac{1}{2}O_2(g) = CO(g)$$

Such an expression is given below (eq 18). The equivalence between eq 10 and 18 is shown in the Appendix section. Upon combining eq 7, 8, and 10, we obtain

$$I(R_{ex} + R_{el} + R_i) = \frac{RT}{4F} \ln\left(\frac{p_{O_{2,c}}}{p_{O_{2,a}}}\right) \tag{11}$$

or, equivalently,

$$I(R_{ex} + R_{el} + R_i) = \frac{RT}{4F} \ln \frac{y_c^0(1 - x_c)[(1 + x_a)(a + x_c) + ab]P_c}{(1 - y_c^0 x_c)(1 - x_a)(a - x_c)P_a} \tag{12}$$

where $a = N_2 y_a^0 / N_1 y_c^0$, $b = (1 - y_a^0)/y_a^0$, and P is the cathode (c) or anode (a) total pressure.

The energy balance for the whole reactor (Figure 1b) reads

$$N_1\bar{C}_{p,g}[(T_c - T_1) - (T_c - T_0)y_c^0 x_c] + N_2\bar{C}_{p,g}\left\{(T_a - T_2) + (T_a - T_0)\left[y_a^0 x_a + \frac{N_1}{N_2}y_c^0 x_c(1 + x_a)\right]\right\} + N_3\bar{C}_{p,s}\left\{(T_a - T_3) - 2x_a(T_a - T_0)\left[\frac{N_1}{N_3}y_c^0 x_c + \frac{N_2}{N_3}y_a^0\right]\right\} + (UA)_c(T_c - T^c) + (UA)_a(T_a - T^c) = 2(N_1 y_c^0 x_c + N_2 y_a^0)x_a(-\Delta H_0) - EI \tag{13}$$

where T_1, T_2, and T_3 are the feed temperatures of the cathodic air, anodic air, and carbon feed streams, respectively, T_c and T_a are the cathode and anode temperatures, UA denotes the product of the overall heat-transfer coefficient times external heat-transfer area in the cathode (c) and anode (a), T^c is the ambient temperature, T_0 is the reference temperature, and $-\Delta H_0$ is the standard enthalpy change, at T_0, for the reaction

$$C(s) + \tfrac{1}{2}O_2(g) \rightarrow CO(g)$$

In order to simplify the notation, we have assumed a constant molar heat capacity for all gas streams ($\bar{C}_{p,g}$); $\bar{C}_{p,s}$ is the heat capacity of the solid carbon. Actual calculations, of course, were performed taking into account both the temperature and the composition dependence of all heat capacities.

The right-hand side of eq 13 is the electrochemical equivalent of the usual "heat generation" term encountered in conventional reactor theory. Upon rearrangement, we obtain

$$2x_a(-\Delta H_0)(N_1 y_c^0 x_c + N_2 y_a^0) - EI = \frac{I}{2F}(-\Delta H_0)(x_a - \eta + \gamma) \tag{14}$$

where η, commonly referred to as efficiency (Bockris and Reddy, 1970; Debenedetti and Vayenas, 1983; Vayenas et al., 1985), is the ratio of actual to "thermoneutral" voltages,

$$\eta = \frac{E}{E_{th}} = \frac{E}{(-\Delta H_0)/2F} \tag{15}$$

and $\gamma = N_2 y_a^0 x_a/(I/4F)$ is the ratio of chemical to electrochemical oxygen consumption. The steady-state energy balance therefore reads

$$N_1\bar{C}_{p,g}[(T_c - T_1) - (T_c - T_0)y_c^0 x_a] + N_2\bar{C}_{p,g}\left\{(T_a - T_2) + (T_a - T_0)\left[y_a^0 x_a + \frac{N_1}{N_2}y_c^0 x_c(1 + x_a)\right]\right\} + N_3\bar{C}_{p,s}\left\{(T_a - T_3) - 2x_a(T_3 - T_0)\left[\frac{N_1}{N_3}y_c^0 x_c + \frac{N_2}{N_3}y_a^0\right]\right\} + (UA)_c(T_c - T^c) + (UA)_a(T_a - T^c) = \frac{I}{2F}(-\Delta H_0)(x_a - \eta + \gamma) \tag{16}$$

where the left-hand side is the heat removal term and the right-hand side is the heat generation term. Finally we write an energy balance around the cathode, in order to relate T_c and T_a,

$$N_1\bar{C}_{p,g}(T_c - T_1) + (UA)_{el}(T_c - T_a) + (UA)_c(T_c - T^c) = 0 \tag{17}$$

where $(UA)_{el}$ is the product of the overall cathode–anode heat-transfer coefficient times electrolyte cross-sectional area normal to anion flow.

The governing equations that describe the reactor's steady-state operation are therefore the two material balances (eq 5 and 6), the Nernst-Khirchoff relationship (eq 12), the energy balances (eq 16 and 17), and the rate expression (eq 4).

Numerical Scheme. The governing equations were solved numerically according to the following iterative scheme: (i) choose an anode temperature (T_a), and calculate the cathode temperature (T_c) from eq 17; (ii) assume x_c; (iii) solve eq 6 for x_a (with right-hand side as per eq 4); (iv) solve eq 12 for x_c (with I as per eq 5); (v) return to (ii) until convergence between assumed and calculated x_c is achieved; (vi) return to (i).

Step (iii) was solved by applying regular perturbation (Nayfeh, 1973) to the fourth-order eq 6. Equation 12 [i.e., step (iv)] was solved with Newton–Raphson's method. Thus, for each imposed anodic temperature, we solved the coupled kinetic–material–electrical eq 4–16 and 12 iteratively. Steady states correspond to the particular choice of anode temperature for which the energy balance is satisfied. Since the anodic temperature was chosen as an independent variable, the range of bath temperatures explored includes unphysically low values, for which the anode would not exist as a liquid. Clearly, we are interested only in those steady states for which the assumption

Table I. Base Case Operating Parameters and Physical Properties

$N_1 = 8 \times 10^{-6}$ mol/s	$\delta = 2 \times 10^{-3}$ m
$N_2 = 6 \times 10^{-6}$ mol/s[a]	$R_{el} = 0.5\ \Omega$
$N_3 = 3.2 \times 10^{-5}$ mol/s	$R_{ex} = 0.5\ \Omega$
$y_c^0 = 1$	$T^c = 298$ K
$y_a^0 = 1$	$T_0 = 298$ K
$y_s^0 = 0.9$	$T_{feed} = 900$ K
$A_{el} = 1.6 \times 10^{-3}$ m^2	$(UA)_c = 1.26 \times 10^{-1}$ J/(h K)
$V_a = 6.4 \times 10^{-5}$ m^3	$(UA)_a = 1$ J/(h K)
$U_{el} = 20$ J/(s m^2 K)	$k_r^\infty = 10^5$ m^3/(mol s)
$E_r = 125.4$ kJ/mol	$\rho_{Fe} = 7.26 \times 10^6$ g/m^3
$\bar{C}_{p,g}{}^0 = 31.38$ J/(mol K)[b]	$\bar{C}_{p,s}{}^0 = 15.9$ J/(mol K)[b]
$\bar{C}_{p,g} = 37.45$ J/(mol K)[c]	$\bar{C}_{p,s} = 24.7$ J/(mol K)[c]

[a] $N_2 = 0$ whenever $y_a^0 = 0$. [b] Inlet composition, temperature average between T_0 and T_{feed}. [c] Outlet composition, temperature average between T_0 and T_a.

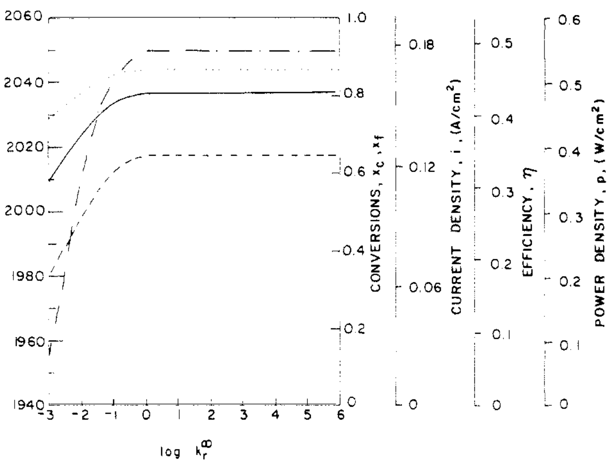

Figure 2. Effect of assumed reaction rate preexponential factor (k_r^∞) upon anodic temperature, T_a (-··-); cathodic oxygen conversion, x_c, current density, i, and efficiency, η (—); carbon conversion, x_f (···); and power density, p (- - -). $T_{feed} = 750$ K, $R_{el} = 0.1\ \Omega$. Other conditions as per Table I.

of a fused iron bath reactor is verified.

Results and Discussion

Values of the geometic and operating parameters used as a base case for the present calculations are listed in Table I. The variables that were found to affect reactor performance more significantly were anodic oxygen feed, external load. They are discussed separately below. First, however, we address the influence of the assumed reaction rate constant (k_r) upon our calculations.

Kinetic Parameters. Figure 2 shows the effect of k_r^∞ upon steady-state anodic temperature (T_a), cathodic oxygen conversion (x_c), current density (i), and efficiency (η). For an activation energy, E_r, of 125.4 kJ/mol, equilibrium is attained for $k_r^\infty > 1$ m^3/(mol·s). This implies that for a conservatively low k_r^∞ of 10^5 m^3/(mol·s), characteristic of liquid-phase second-order reactions (Smith, 1970), the fused bath cell operates arbitrarily close to equilibrium. Throughout this work, we have used $k_r^\infty = 10^5$ m^3/(mol·s) and $E_r = 125.4$ kJ/mol. The results are insensitive to changes in kinetic parameters for any realistic choice of k_r^∞ and E_r (for $k_r^\infty = 10^5$ m^3/(mol·s), no change in operating conditions or performance indicators was detected when E_r was varied over the range 25 kJ/mol < E_r < 300 kJ/mol). It should also be noted that the liquid-phase gasification involves atomic oxygen as a reactant and should therefore possess a much higher k_r^∞ value than the one assumed here. Hence, for all practical purposes, the cell operates at equilibrium. We have verified the latter statement in calculations in which eq 6 was replaced by

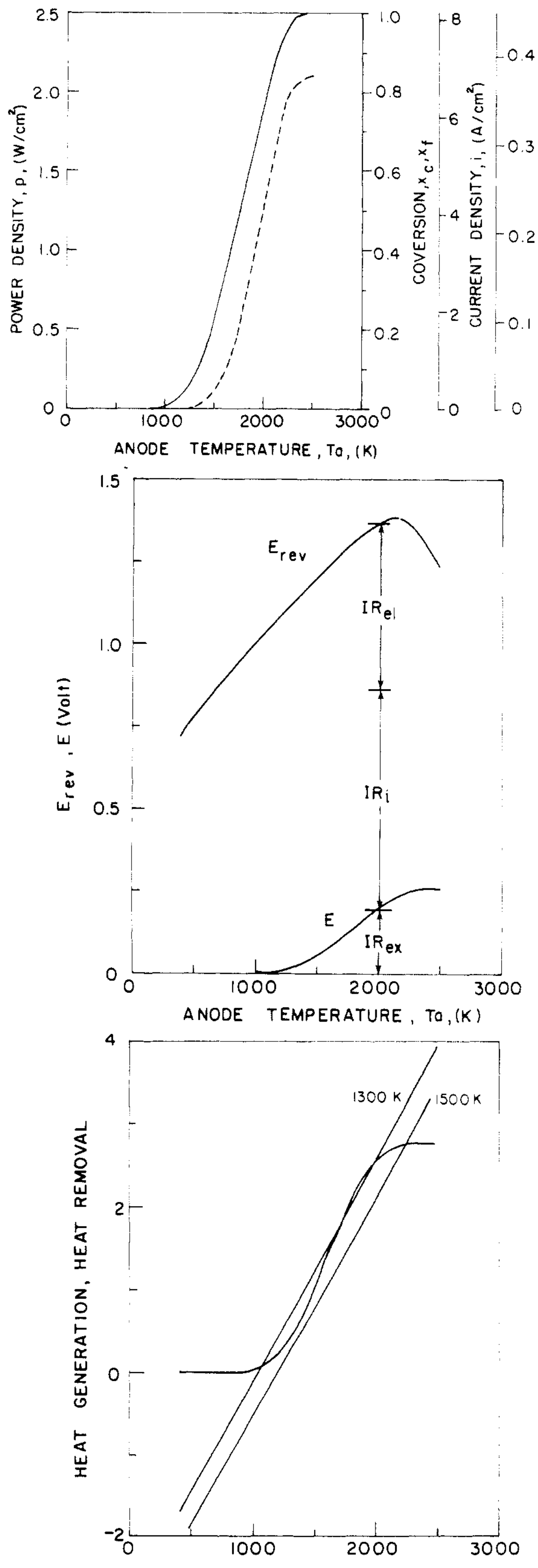

Figure 3. (a) Effect of anode temperature upon cathodic oxygen and carbon conversions, x_c and x_f, current density, i, and efficiency, η (—); and power density, p (- - -). $T_{feed} = 1300$ K, $N_1 = 1.6 \times 10^{-3}$ mol s^{-1}, $N_2 = 0$, $N_3 = 74.67 \times 10^{-5}$ mol s^{-1}, $y_c^0 = 0.21$, $R_{ex} = 2 \times 10^{-3}\ \Omega$, $R_{el} = 5 \times 10^{-3}\ \Omega$, $(UA)_c = 1.26 \times 10^{-2}$ J/(h K), $(UA)_a = 0.1$ J/(h K). Other conditions as per Table I. (b) Effect of anode temperature upon open-circuit and operating voltages. Conditions as per a. (c) Heat generation and removal rates (in units of $N_1\bar{C}_{p,g}T_1$) as a function of anode temperature. Conditions as per a. Labels are feed temperatures.

the equilibrium condition: no changes in conversion, voltage, current, or power density resulted.

Current and Power Generation. In Figure 3a we show the dependence of cathodic oxygen and carbon conversions (x_c, x_f), current density (i), efficiency (η), and power density (p) upon anode temperature. The extremely high power and current densities illustrate the benefits that can be obtained by minimizing ohmic losses at the electrodes. Recent progress in the development of $La_{1-x}Sr_xMnO_3$ ($0 \leq x \leq 0.5$) or $La_{1-y}Ca_yMnO_3$ ($0 < y < 0.6$) (perovskite-type) films with resistivities on the order of 4×10^{-3} Ω·cm at 1000 °C (Brown, 1986) allows the attainment of very low electrode resistances. These can be further minimized by introducing a sufficiently high number of metallic current collectors. For purely ohmic polarization, it follows immediately from eq 7 and 8 that power production is maximized when the external load equals the sum of internal and electrode losses ($R_i + R_{el}$). Consequently, when the cell is operated under high current density conditions, R_{ex} should be as low as possible and comparable to ($R_i + R_{el}$). Figure 3b shows the temperature dependence of the reversible and actual cell voltage for the same conditions as per Figure 3a. For given values of the electrode and electrolyte resistances, the difference between both curves is proportional to the current (eq 7).

The cell's open-circuit voltage can be written (see Appendix section) as

$$2FE_{rev} = -\Delta H_0 + T\left[\Delta S_0 - R \ln \frac{\alpha_{CO}}{{\alpha_{O_2}}^{1/2}}\right] \qquad (18)$$

where we have taken the activity of solid carbon to be unity and ΔH_0 and ΔS_0 refer to the reaction

$$C(s) + \tfrac{1}{2}O_2(g) = CO(g)$$

Since ΔS_0 is positive in our case, E_{rev} will, in principle, increase with temperature. At very high oxygen conversions, however, the logarithmic term in eq 18 becomes important and E_{rev} can exhibit a maximum: this is the behavior shown in Figure 3b. Upon combining eq 7 and 8, we obtain

$$I = \frac{E_{rev}}{R_{el} + R_{ex} + R_i} \qquad (19)$$

Since R_i is a strongly decreasing function of temperature (eq 9), the sign of dI/dT, which is that of $d \ln E_{rev}/dT - (R_{ex} + R_{el} + R_i)^{-1}\, dR_i/dT$, will, in general, be positive. Thus, cathodic oxygen conversion, x_c (see eq 5), power output (I^2R_{ex}), operating voltage (IR_{ex}), and efficiency [$IR_{ex}/(-\Delta H_0/2F)$] will also, in general, be monotonically increasing functions of temperature. This behavior (see Figure 3a) is fundamentally different from the one that characterizes other fuel cell reactions, such as CO oxidation (Debenedetti and Vayenas, 1983) in which $\Delta S_0 < 0$. In that case, it can be shown from an analysis identical with the preceding one, that conversion, power, current ouput, and efficiency exhibit maxima as a function of temperature. This means that, because the present process involves a reaction with positive entropy change, the benefits of high-temperature operation are not only kinetic (lower activation polarization and electrolyte resistance) but also thermodynamic (since $-\Delta G_0$ increases with temperature and so, in principle, will E_{rev}). The electrolyte thickness assumed in this study (2 mm) is conservatively high. Accordingly, E values higher than those shown in Figure 3b appear possible in an actual fuel cell.

Figure 3c illustrates the solution of the coupled material and energy balances for the same operating conditions as in Figure 3a,b and two different feed temperatures. The S-shaped curve is the right-hand side of eq 16, the energy balance, and is thus the electrochemical analogue of the usual heat generation function in chemical reaction engineering, in units of $N_1\bar{C}_{p,g}T_1$. The straight line is the left-hand side of eq 16 (in units of $N_1\bar{C}_{p,g}T_1$) and constitutes the usual heat removal term. At the ignited steady state corresponding to the highest feed temeprature, the cell produces 19.6 kW/m^2, at a current density of 7.84 A/cm^2, and an operating voltage of 0.25 V. The gasification rate is 1462 mol of CO/(h·m^2) (i.e., 33 m^3(STP)/(h·m^2)), and the air and carbon feeds are 81 m^3(STP)/(h·m^2) and 20 kg/(h·m^2), respectively (all specific values are per electrolyte area normal to anion flow). In light of what has been said above regarding concentration overpotentials, these figures are best-case estimates. In the calculations that follow, we use significantly lower current densities.

Effect of Anodic Oxygen Feed. Anodic oxygen feed can be used in the fused bath process to provide part of the heat of reaction needed to sustain steady operation at high temperature. Figure 4a shows the effect of anodic oxygen feed upon power density (p), carbon conversion (x_f), cathodic oxygen conversion (x_c), current density (i), and efficiency (η). These quantities are all obtained from the solution of the coupled material balance and electrical equations, with temperature as an independent variable. It follows from Figure 4a that, for a given anodic temperature, carbon consumption (and therefore CO production) is very sensitive to anodic oxygen feed, whereas electrochemical oxygen consumption (and therefore current and power densities) is, on the other hand, relatively insensitive to y_a^0. Since, however, T_a is not independently variable under actual operating conditions, we must first determine the influence of y_a^0 upon anode temperature in order to assess the true importance of anodic oxygen feed upon cell performance.

Figure 4b illustrates the behavior of the heat generation and heat removal functions as y_a^0 is varied (same conditions as in Figure 4a). It is obvious that the amount of oxygen fed directly into the anode has a profound influence upon the heat generation function (and hence upon the reactor's temperature). Upon repeating the calculation of the complete set of coupled electrical, material, and energy balance equations for different values of y_a^0 (with other conditions constant as per Figure 4a,b) we obtain Figure 4c. We can conclude from this calculation that manipulation of y_a^0 allows, in principle, an extremely sensitive control of cell performance. This is of obvious importance from a reactor operation viewpoint.

Extrema in the heat generation function are an interesting feature of electrochemical reactors. If I is a monotonically increasing function of temperature (i.e., in general, if $\Delta S_0 > 0$), it follows immediately from the energy balance (eq 16) that the heat generation reaches a maximum for a value of the current $I^* = (-\Delta H_0)/4FR_{ex}$, assuming $x_a \approx 1$, an excellent approximation in the present case. If, on the other hand, I is not a monotonically increasing function of temperature, that is to say, in general, $\Delta S_0 < 0$, the heat generation function can exhibit even more interesting behavior; this case, however, falls beyond the scope of this paper.

Effect of External Load. Figure 5a illustrates the effect of the external load upon cathodic oxygen conversion (x_c), carbon conversion (x_f), and current and power densities (i, p). As was the case with Figure 4a, the curves were obtained by solving the material balance and electrical equations, with temperature as the independent variable.

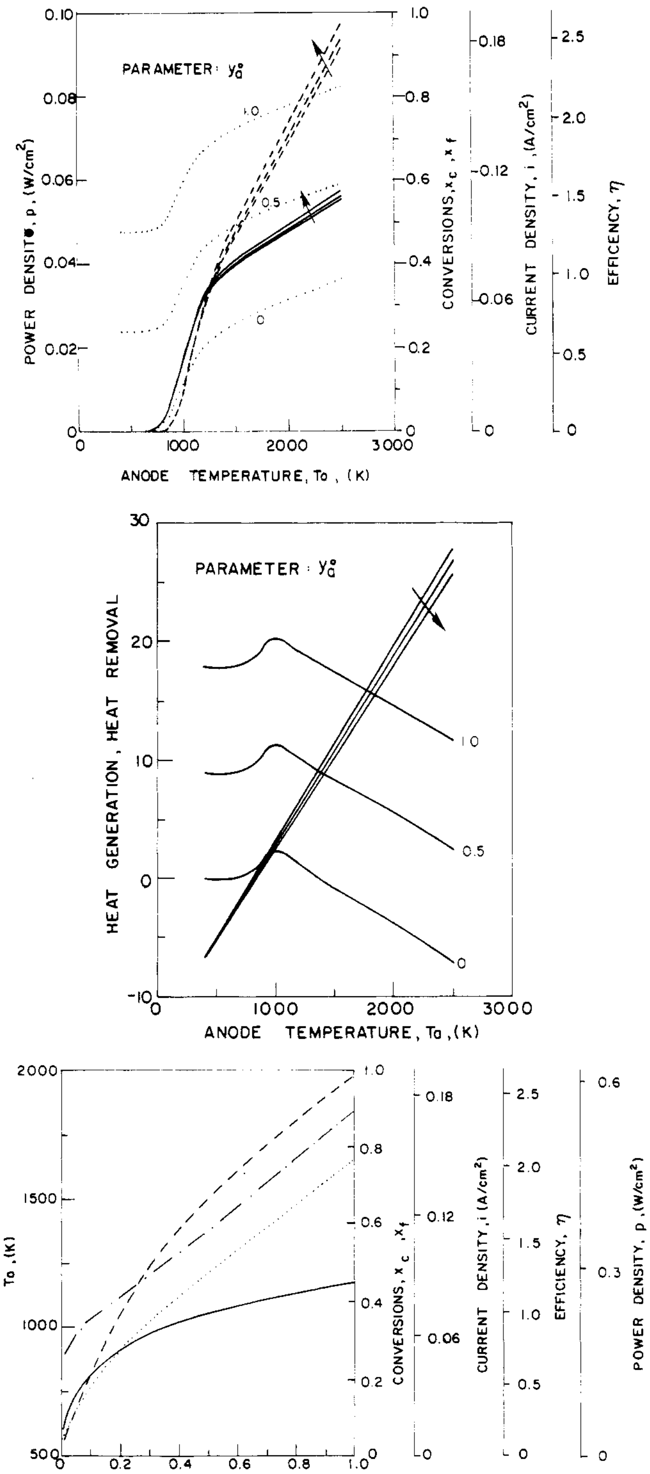

Figure 4. (a) Effect of anode temperature upon cathodic oxygen conversion, x_c, current density, i, and efficiency, η (—); carbon conversion, x_f (···); and power density, p (- - -), for several values of the mole fraction of oxygen in the anodic gas feed (y_a^0). $N_3 = 2.8 \times 10^{-5}$ mol/s, $T_{feed} = 1000$ K, $(UA)_c = 0.025$ J/(h K), $(UA)_a = 0.2$ J/(h K). Other conditions as per Table I. The arrow indicates the direction of increasing y_a^0. (b) Behavior of heat generation and heat removal functions for several values of the mole fraction of oxygen in the anodic gas feed (y_a^0). Conditions as per a. The arrow indicates the direction of increasing y_a^0. (c) Effect of anodic oxygen feed (y_a^0) upon steady-state anodic temperature, T_a (–·–), cathodic oxygen conversion, x_c, current density, i, and efficiency, η (—); carbon conversion, x_f (···); and power density, p (- - -). Conditions as per a.

It is obvious from Figure 5a that cathodic oxygen conversion (i.e., current flow) can be virtually eliminated by increasing the load. Carbon conversion, on the other hand,

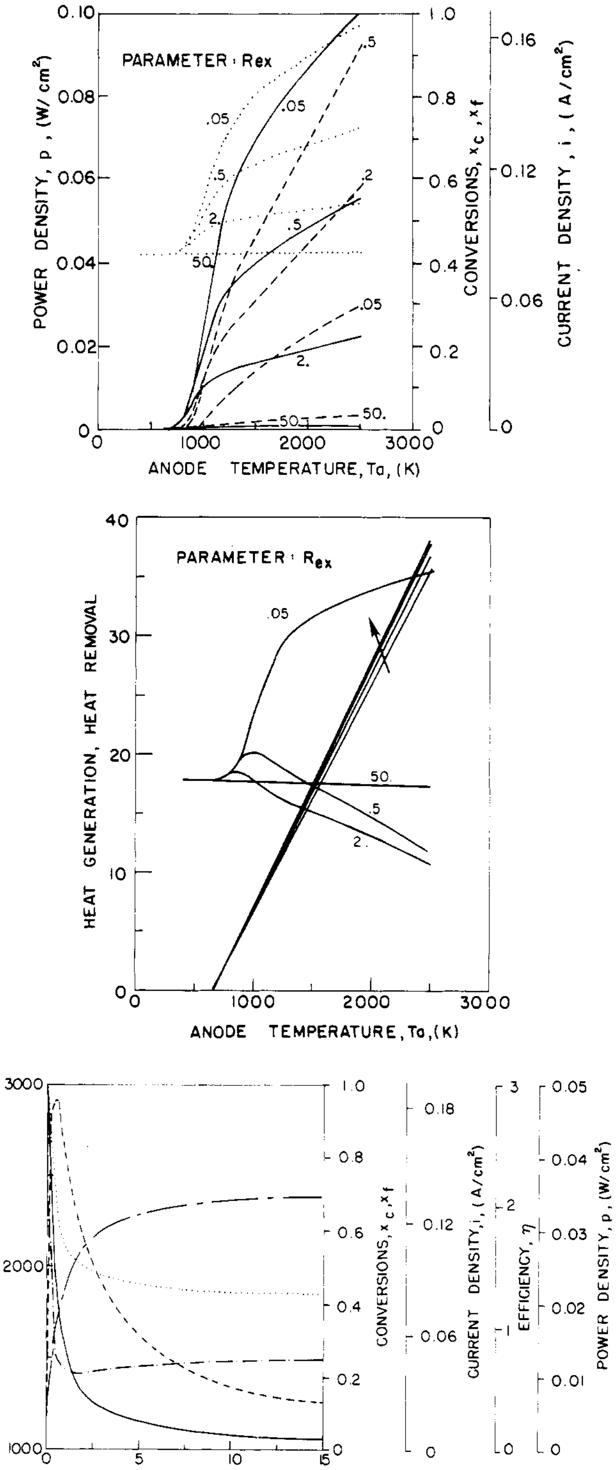

Figure 5. Effect of anode temperature upon cathodic oxygen conversion, x_c, current density, i (—); carbon conversion, x_f (···); and power density, p (- - -), for several values of the external load, R_{ex}. Conditions as per Table I. (b) Behavior of heat generation and heat removal functions for several values of the external load, R_{ex}. Arrow indicates the direction of increasing R_{ex}. Conditions as per Table I. (c) Effect of external load (R_{ex}) upon steady-state anodic temperature, T_a (–·–); cathodic oxygen conversion, x_c, and current density, i (—); carbon conversion, x_f (···); efficiency, η (– – –); and power density, p (- - -). Conditions as per Table I.

remains finite in this example due to the presence of direct anodic oxygen feed. Another important observation is the fact that the cell's power exhibits a maximum with respect to R_{ex} at every temperature. This maximum, as was previously noted, corresponds to the condition $R_{ex} = R_{el} + R_i$ for purely ohmic polarization.

Figure 5b illustrates the effect of changes in the external load upon the macroscopic energy balances and hence upon the fuel cell's operating point. For any given anodic temperature and assuming $x_a \approx 1$, the heat generation is composed of three terms,

$$\text{heat generation} \approx \frac{(-\Delta H_0)I}{2F} - I^2R_{ex} + 2N_2y_a^0(-\Delta H_0) \tag{20}$$

Since, moreover, $I \propto (R_{ex} + R_{el} + R_i)^{-1}$ (see eq 19), the heat generation is not monotonic in R_{ex}: this is the behavior shown in Figure 5b.

The effects of R_{ex} upon the fuel cell's steady-state operating characteristics are shown in Figure 5c. The minimum in the anode temperature curve (i.e., T_a) is a direct consequence of the nonmonotonic behavior of the heat generation function (see Figure 5b). The monotonic decrease in i (and other quantities directly proportional to i) is a consequence of the fact that increasing the external load outweighs competing effects, such as the mild increase in T_a for $R_{ex} \geq 1\ \Omega$. The maximum in power output with respect to R_{ex}, on the other hand, follows trivially from writing $p = I^2R_{ex}/A_{el}$ and monotonically decreasing behavior of i with respect to R_{ex}. It is clear from this discussion that R_{ex} is a variable of fundamental importance in controlling reactor performance. This is advantageous in light of the ease with which the external load can be manipulated.

Steady-State Multiplicity. It follows from the shape of the energy balance versus temperature relationship (see Figures 3c, 4b, and 5b) that the well-mixed fused bath cell can exhibit steady-state multiplicity under a wide variety of operating conditions. This feature of well-mixed fuel cell behavior has already been analyzed in detail (Debenedetti and Vayenas, 1983). In general, steady-state multiplicity is suppressed by increasing the anodic oxygen feed (Figure 4b), increasing the external load (Figure 5b), or increasing the feed flow rate.

Steady-state multiplicity is more appropriately displayed in anodic versus feed temperature coordinates (Figure 6), where a $T_a = T_{feed}$ isothermal line has been included for reference. Curve a is a base case. It can be seen that an increase in anodic oxygen feed causes the gradual disappearance of multiplicity (curves b and c), while, at the same time, the anode's temperature is shifted toward higher values. Similarly, an increase in external load, ohmic losses at the electrodes, or in feed flow rates also tends to suppress steady-state multiplicity (curves d–f), but this is done through a "quenching" of the heat generation function, and therefore a decrease in anodic temperature occurs.

Conclusions

The gasification of coal with simultaneous generation of electricity in a new solid electrolyte fuel cell with a fused iron bath anode is a promising concept. The process combines the advantages of coal gasification in molten metal baths (high gasification efficiency, production of low-sulfur gas) with the thermodynamic efficiency of high-temperature fuel cells. The oxidation of coal to carbon monoxide, furthermore, is accompanied by a positive entropy change. This leads to current and power densities which, in general, tend to be monotonically increasing functions of temperature. Operation at the high temperatures necessary to maintain a molten anode is thus convenient not only from a kinetic viewpoint (negligible activation overpotential) but also for thermodynamic reasons.

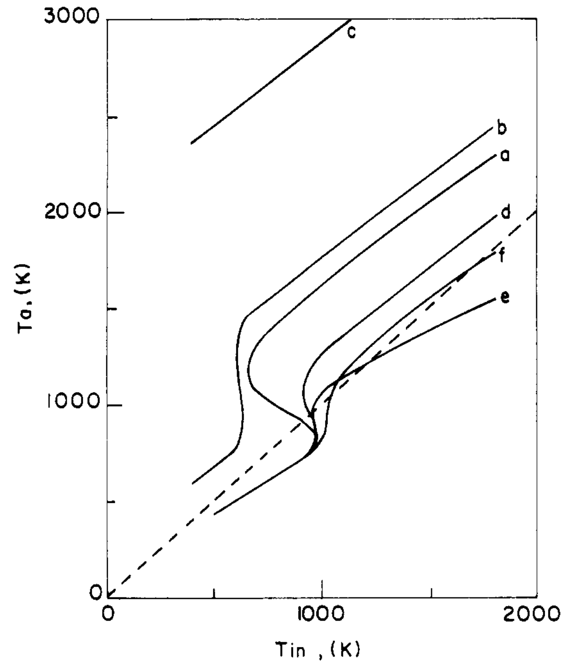

Figure 6. Influence of operating parameters upon steady-state multiplicity. Curve a: base case, $N_2 = 0$, $N_3 = 2.8 \times 10^{-5}$ mol/s, $R_{ex} = 0.1\ \Omega$, $(UA)_c = 1.26 \times 10^{-2}$ J/(h K), $(UA)_a = 0.1$ J/(h K). Other conditions as per Table I. Curves b, c: effect of anodic oxygen feed; $N_2 = 6 \times 10^{-6}$ mol/s, $y_a^0 = 0.21$ (b), $y_a^0 = 1$ (c). Curve d: effect of electrode resistance; $R_{el} = 0.1\ \Omega$. Curve e: effect of external load; $R_{ex} = 0.3\ \Omega$. Curve f: effect of flow rates; $N_1 = 1.6 \times 10^{-5}$ mol/s, $N_3 = 3.5N_1$. The dashed line is a reference $T_a = T_{feed}$ condition.

A lumped parameter model of the elementary cell shows that the reactor can produce ca. 33 m^3 (STP) of CO/(h·m^2), with current and power densities of 7.8 A/cm^2 and 19.6 kW/m^2. Low ohmic losses at the electrodes are essential for the attainment of these high production rates. These numbers represent best-case estimates, since the model assumes negligible concentration polarization, certainly an idealization at these high current densities. The most important parameters affecting reactor performance were found to be anodic oxygen feed, external load, and electrode resistance, the first two of which are easily manipulated process variables and can therefore be used to control cell performance. External load controls the reactor's electrical power generation, and anodic oxygen feed controls the reactor's operating temperature.

The steady-state analysis reveals a variety of interesting phenomena, such as ignition–extinction, steady-state multiplicity, and extrema in the heat generation function. The lumped parameter model has been used here to investigate the performance of a single elementary cell. An obvious extension of this work is to study the performance of a battery of cells, exploring the relative merits of possible hydraulic and electrical configurations. It is also important to study the influence of diffusional limitations by relaxing the perfect mixing assumption and introducing cell geometry explicitly into the overall picture. Work is now in progress on both of these problems.

Although the fused iron bath fuel cell idea is certainly an attractive one, and although the present calculations are indeed encouraging, the reactor needs to be tested experimentally. Only then will the true merits and limitations of this novel concept become apparent.

Acknowledgment

We are grateful to Professor Costas Vayenas for several helpful discussions.

Nomenclature

A_a = anodic heat loss area, m^2
A_c = cathodic heat loss area, m^2
A_{el} = superficial electrode area normal to anion flow, m^2
a = ratio of anodic to cathodic oxygen flux, $N_2 y_a{}^0/N_1 y_c{}^0$, dimensionless
b = ratio of inert to oxygen mole fraction in anode feed, $(1 - y_a{}^0)/y_a{}^0$, dimensionless
$\bar{C}_p$ = temperature- and composition-averaged specific heat, J/(mol·K)
E_r = activation energy for the reaction $\underline{C} + \underline{O} \rightarrow CO(g)$, kJ/mol
E_{rev} = open-circuit voltage, V
E_{th} = thermoneutral voltage $(-\Delta H_0)/nF$, V
F = Faraday's constant, 96 484 C/equiv
I = current, A
i = current density, A/m^2
$K_{\underline{C}}$ = equilibrium constant for the reaction C(graphite) = $\underline{C}$ (in Fe), dimensionless
K_e = equilibrium constant for the reaction C(graphite) + $\underline{O}$ = CO(g), dimensionless
K_g = equilibrium constant for the reaction C(graphite) + $^1/_2O_2(g)$ = CO(g), dimensionless
$K_{\underline{O}}$ = equilibrium constant for the reaction $^1/_2O_2(g) = \underline{O}$ (in Fe), dimensionless
k_r = forward reaction rate constant for the reaction $\underline{C} + \underline{O}$ = CO, $m^3/(mol{\cdot}s)$
k'_r = reverse reaction rate constant for the reaction $\underline{C} + \underline{O}$ = CO, s^{-1}
$k_r{}^\infty$ = preexponential factor of reaction rate constant k_r, $m^3/(mol{\cdot}s)$
N = feed stream molar flow rate, mol/s
P = total pressure, N/m^2
p = power density, W/m^2, or partial pressure, N/m^2
R = gas constant, 8.3144 J/(mol·K)
R_{el} = electrode resistance, Ω
R_{ex} = external load, Ω
R_i = electrolyte resistance, Ω
r = reaction rate, $mol/(m^3{\cdot}s)$
T = absolute temperature, K
U = overall heat-transfer coefficient, $W/(m^2{\cdot}K)$
V_a = anodic volume, m^3
x = conversion, dimensionless
y = mole fraction, dimensionless
z = equilibrium carbon mole fraction in the fused anode, dimensionless

Greek Symbols

α = activity, dimensionless
γ = ratio of chemical to electrochemical oxygen consumption, dimensionless, or activity coefficient, $(\%\ wt)^{-1}$
ΔG_0 = standard Gibbs energy change for a given reaction, J/mol
ΔH_0 = standard enthalpy change for a given reaction, J/mol
ΔS_0 = standard entropy change for a given reaction, J/mol
δ = electrolyte thickness, m
η = efficiency, dimensionless
μ = chemical potential, J/mol
$\bar{\mu}$ = electrochemical potential, J/mol
ρ = density, g/m^3
ϕ_1, ϕ_2 = coefficients defined in eq 4, mol/m^3

Subscripts

0 = reference or standard conditions
1 = cathodic gas feed stream
2 = anodic gas feed stream
3 = anodic solid feed stream
a = anode
c = cathode
e = electron
f = fuel
g = gas
l = liquid
s = solid
– = atomic oxygen or dissolved carbon

Superscripts

0 = feed conditions
c = ambient conditions

Appendix

The carbon concentration in the fused bath was calculated from the expression (Chipman, 1970; Rao, 1985)

$$\log\left(\frac{z}{1-2z}\right) + \frac{1180}{T} - 0.87 + \left(0.72 + \frac{3400}{T}\right)\left(\frac{z}{1-z}\right) = 0 \quad \text{(A-1)}$$

where z is the mole fraction of carbon corresponding to the equilibrium

$$\text{C(graphite)} = \underline{\text{C}} \text{ (in Fe)} \quad \text{(A-2)}$$

For the oxygen dissolution, we write (Sigworth and Elliott, 1974)

$$^1/_2O_2(g) = \underline{O} \text{ (in Fe)} \qquad \Delta G_0 = -1.17 \times 10^5 - 2.89T \quad \text{(J/g-atom)} \quad \text{(A-3)}$$

and, for the gasification (Gaskell, 1981),

$$\text{C(graphite)} + {}^1\!/_2O_2(g) \rightarrow CO(g) \qquad \Delta G_0 = -1.17 \times 10^5 - 84.87T \quad \text{(J/g-atom)} \quad \text{(A-4)}$$

where the standard state for dissolved atomic oxygen is an ideal 1 wt % solution in molten Fe. Let the equilibrium constants for reactions A-2, A-3, and A-4 be $K_{\underline{C}}$, $K_{\underline{O}}$, and K_g, respectively. Reactions A-2 and A-3 were assumed to be in equilibrium throughout. In order to arrive at eq 4, we write

$$r = k_r[\underline{O}][\underline{C}] - k'_r[CO] \quad \text{(A-5)}$$

where

$$[\underline{O}] = \phi_1[\%\underline{O}] \quad \text{(A-6)}$$

$$[\underline{C}] = \phi_2[\%\underline{C}] \quad \text{(A-7)}$$

We then invoke the equilibrium conditions for oxygen and carbon,

$$[\%\underline{O}] = p_{O_2}{}^{1/2}K_{\underline{O}} \quad \text{(A-8)}$$

$$\gamma_{\underline{C}}[\%\underline{C}] = K_{\underline{C}} \quad \text{(A-9)}$$

where γ is here an activity coefficient and where ideal behavior has been assumed for oxygen ($\alpha_{\underline{O}} = \gamma_{\underline{O}}[\%\underline{O}] = [\%\underline{O}]$; Winkler and Bakish, 1971; Gaskell, 1981; Rao, 1985). The reverse reaction constant, k'_r, is given by

$$k'_r = \frac{RT\phi_1\phi_2}{K\gamma_{\underline{C}}}k_r \quad \text{(A-10)}$$

where K is the equilibrium constant for the reaction $\underline{C} + \underline{O}$ = CO(g) (i.e., $K = K_g/K_{\underline{O}}{}^{-1}K_{\underline{C}}{}^{-1}$). Combining eq A-5–A-7, A-9, and A-10, we obtain, finally,

$$r = k_r[\%C]\left\{[\%\underline{O}] - \frac{y_{CO}}{K_e}\right\}\phi_1\phi_2 \quad (4)$$

where K_e is the equilibrium constant for the reaction C(graphite) + $\underline{O}$ = CO(g) (i.e., $K_e = K_g/K_{\underline{O}}{}^{-1}$).

In order to derive the two equivalent open-circuit voltage expressions (eq 10 and 18), we write the following equilibrium conditions:

$$2\bar{\mu}_{e^-(c)} + {}^1/_2\mu_{O_2(c)} = \bar{\mu}_{O^{2-}(c)} \quad \text{(A-11)}$$
$$\bar{\mu}_{O^{2-}(c)} = \bar{\mu}_{O^{2-}(a)} \quad \text{(A-12)}$$
$$\bar{\mu}_{O^{2-}(a)} = \mu_{\underline{O}(a)} + 2\bar{\mu}_{e^-(a)} \quad \text{(A-13)}$$
$$\mu_{\underline{O}(a)} + \mu_{\underline{C}(l,a)} = \mu_{CO(g,a)} \quad \text{(A-14)}$$
$$\mu_{C(s)} = \mu_{\underline{C}(l,a)} \quad \text{(A-15)}$$
$${}^1/_2\mu_{O_2(g,a)} = \mu_{\underline{O}(a)} \quad \text{(A-16)}$$

which correspond, respectively, to the cathodic half-reaction (eq A-11), equilibration of the anion across the solid electrolyte (eq A-12), anodic half-reaction (eq A-13), oxidation of dissolved carbon (eq A-14), dissolution of carbon (eq A-15), and equilibration of anodic oxygen (eq A-16). Then, from eq A-11–A-13, we obtain

$$2FE_{\text{rev}} = 2[\bar{\mu}_{e^-(a)} - \bar{\mu}_{e^-(c)}] = \frac{1}{2}\mu_{O_2(c)} - \mu_{\underline{O}(a)} \quad \text{(A-17)}$$

which, when combined with eq A-16, yields

$$E_{\text{rev}} = \frac{RT}{4F} \ln \left(\frac{p_{O_2,c}}{p_{O_2,a}} \right) \quad (10)$$

To transform this concentration cell form into eq 18, we combine eq A-17 with eq A-14–A-16

$$2FE_{\text{rev}} = 2[\bar{\mu}_{e^-(a)} - \bar{\mu}_{e^-(c)}] = {}^1\!/_2\mu_{O_2(c)} - \mu_{CO(g,a)} + \mu_{C(s)} \quad \text{(A-18)}$$

and define

$$\mu_{O_2(g)} = \mu^\circ{}_{O_2(g)} + RT \ln \alpha_{O_2} \quad \text{(A-19)}$$

$$\mu_{CO(g)} = \mu^\circ{}_{CO(g)} + RT \ln \alpha_{CO} \quad \text{(A-20)}$$

$$\mu_{C(s)} = \mu^\circ{}_{C(s)} + RT \ln \alpha_C \quad \text{(A-21)}$$

Combining eq A-18–A-21 and rearranging, we obtain

$$2FE_{\text{rev}} = -\Delta H_0 + T\left[\Delta S_0 - R \ln \frac{\alpha_{CO}}{\alpha^{1/2}{}_{O_2(c)}} \right] \quad (18)$$

or, equivalently,

$$E_{\text{rev}} = E_0 + \frac{RT}{4F} \ln \frac{\alpha_{O_2(c)}}{\alpha^2{}_{CO}} \quad \text{(A-22)}$$

where ΔH_0, ΔS_0, and E_0 are the standard state enthalpy change, entropy change, and voltage corresponding to the reaction

$$C(s) + {}^1\!/_2O_2(g) = CO(g)$$

and we have assumed unit carbon activity.

Finally, we show the thermodynamic equivalence between homogeneous, chemical oxidation of carbon (eq 3), and its heterogeneous, electrochemical counterpart (eq 3a). For the latter process, we write

$$2\bar{\mu}_{e^-(c)} + {}^1/_2\mu_{O_2(c)} = \bar{\mu}_{O^{2-}(c)} \quad \text{(A-11)}$$
$$\bar{\mu}_{O^{2-}(c)} = \bar{\mu}_{O^{2-}(a)} \quad \text{(A-12)}$$
$$\bar{\mu}_{O^{2-}(a)} + \mu_{\underline{C}(l,a)} = \mu_{CO(g,a)} + 2\bar{\mu}_{e^-(a)} \quad \text{(A-23)}$$
$$\mu_{C(s)} = \mu_{\underline{C}(l,a)} \quad \text{(A-15)}$$

Equations A-11, A-12, A-23, and A-15, when combined, yield

$$2FE_{\text{rev}} = 2[\bar{\mu}_{e^-(a)} - \bar{\mu}_{e^-(c)}] = \frac{1}{2}\mu_{O_2(c)} - \mu_{CO(g,a)} + \mu_{C(s)} \quad \text{(A-18)}$$

from which, as was shown above, both eq 18 and A-22 follow at once, upon defining activities as per eq A-19–A-21. Therefore, the heterogeneous and homogeneous pathways are thermodynamically identical.

Registry No. Fe, 7439-89-6; ZrO_2, 1314-23-4; Y_2O_3, 1314-36-9; Pt, 7440-06-4.

Literature Cited

Appleby, A. J. Coal Gasification in Fuel-Cell Applications. *Energy* **1987**, *12*(8/9), 729–745.

Archer, D. H.; Alles, J. J.; English, W. A.; Elican, L.; Sverdrup, E. F.; Zahradnik, R. L. *Fuel Cell Systems*; Gould, R. F., Ed.; Advances in Chemistry 47; American Chemical Society: Washington, DC, 1965; p 332.

Baker, L. A.; Ward, R. G. Reaction of an Iron-Carbon Droplet during Free Fall through Oxygen. *J. Iron Steel Inst.* **1967**, *205*(7), 714–717.

Bebelis, S.; Vayenas, C. G. Non-Faradaic Electrochemical Modification of Catalytic Activity: I. The Case of Ethylene Oxidation on Pt. *J. Catal.* **1989**, in press.

Bockris, J. O'M; Reddy, A. K. N. *Modern Electrochemistry*; Plenum Press: New York, 1970; Vol. 2.

Brown, J. T. High-Temperature Solid-Oxide Fuel Cells (SOFCs). *Energy* **1986**, *11*(1/2), 209–228.

Chipman, J. Thermodynamics of Liquid Fe–C Solutions. *Met. Trans.* **1970**, *1*, 2163–2167.

Chipman, J. Thermodynamics and Phase Diagram of the Fe–C System. *Met. Trans.* **1972**, *3*, 55–63.

Costa, B. A New Industrial Process for the Utilization of Solid Fuels, called High Temperature Cogeneration. Private communication, Naples, Italy, 1987.

Costa, B. U.S. Patent Application 07/096,034, 1988.

Coudurier, L.; Hopkins, D. W.; Wilkomirsky, I. *Fundamentals of Metallurgical Processes*, 2nd ed.; Pergamon Press: Oxford, 1985.

Debenedetti, P. G.; Vayenas, C. G. Steady-State Analysis of High Temperature Fuel Cells. *Chem. Eng. Sci.* **1983**, *38*(11), 1817–1829.

Etsell, T. H.; Flengas, S. N. Overpotential Behavior of Stabilized Zirconia Solid Electrolyte Fuel Cells. *J. Electrochem. Soc.* **1971**, *118*, 1890–1900.

Farr, R. D.; Vayenas, C. G. Ammonia High Temperature Solid Electrolyte Fuel Cell. *J. Electrochem. Soc.* **1980**, *127*(7), 1478–1483.

Franke, M.; Winnick, J. High-Performance Perovskite Cathode for Molten Carbonate Fuel Cell. *J. Electrochem. Soc.* **1988**, *135*(6) 1595–1596.

Frickett, A. P. Fuel Cells for Electric Utility Power Generation. *Adv. Energy Systems Technol.* **1986**, *5*, 1.

Gaskell, D. R. *Introduction to Metallurgical Thermodynamics*, 2nd ed.; McGraw-Hill: New York, 1981.

Kiratzis, N.; Stoukides, M. The Synthesis of Hydrogen Cyanide in a Solid Electrolyte Fuel Cell. *J. Electrochem. Soc.* **1987**, *134*(8), 1925–1929.

Manton, M. Oxidation of Butene over Pt Catalyst in a ZrO_2–Y_2O_3 Electrochemical Reactor. Ph.D. Dissertation, Massachusetts Institute of Technology, Cambridge, 1986.

Metcalfe, I.; Sundaresan, S. Oxygen Transfer between Metals and Oxygen-Ion Conducting Supports. *AIChE J.* **1988**, *34*(2), 195–208.

Michaels, J. N.; Vayenas, C. G. Kinetics of Vapor-Phase Electrochemical Oxidative Dehydrogenation of Ethylbenzene. *J. Catal.* **1984a**, *85*, 477–487.

Michaels, J. N.; Vayenas, C. G. Styrene Production from Ethylbenzene on Platinum in a Zirconia Electrochemical Reactor. *J. Electrochem. Soc.* **1984b**, *131*(11), 2544–2550.

Michaels, J. N.; Vayenas, C. G.; Hegedus, L. L. A Novel Cross-Flow Design for Solid-State Electrochemical Reactors. *J. Electrochem. Soc.* **1986**, *133*(3), 522–525.

Nakagawa, N.; Ishida, M. Performance of an Internal Direct-Oxidation Carbon Fuel Cell and its Evaluation by Graphic Exergy Analysis. *Ind. Eng. Chem. Res.* **1988**, *27*, 1181–1185.

Nakajima, H.; Okane, K.; Furujo, S.; Okamura, S.; Sueyasu, M.; Tanoue, T.; Anezaki, S.; Matsuo, T. Coal Gasification using Molten Iron and its Application to Steelmaking. *Ironmaking Steelmaking*, **1983**, *10*(3), 130–136.

Nayfeh, A. *Perturbation Methods*; John Wiley and Sons: New York, 1973.

Neophytides, S.; Vayenas, C. G. Non-Faradaic Electrochemical Modification of Catalytic Activity. II. The Case of Methanol Dehydrogenation and Decomposition on Silver. *J. Catal.* **1989**, in press.

Nomura, H.; Mori, K. Kinetics of Decarburization of Liquid Iron at Low Concentrations of Carbon. *Trans. ISIJ* **1973**, *13*, 325–332.

Rao, Y. K. *Stoichiometry and Thermodynamics of Metallurgical Processes*; Cambridge University Press: Cambridge, 1985.

Sain, D. R.; Belton, G. R. Interfacial Reaction Kinetics in the Decarburization of Liquid Iron by Carbon Dioxide. *Met. Trans. B* **1976**, *7B*, 235-243.

Sigal, C.; Vayenas, C. G. Ammonia Oxidation to Nitric Oxide in a Solid Electrolyte Fuel Cell. *Solid State Ionics* **1981**, *5*, 567-570.

Sigworth, G. K.; Elliott, J. F. The Thermodynamics of Liquid Dilute Iron Alloys. *Met. Sci.* **1974**, *8*, 298-310.

Smith, J. M. *Chemical Engineering Kinetics*, 2nd ed.; McGraw-Hill: New York, 1970.

Solar, M. Y.; Guthrie, R. I. L. Kinetics of the Carbon-Oxygen Reaction in Molten Iron. *Met. Trans.* **1972**, *3*, 713-722.

Stoukides, M.; Vayenas, C. G. Kinetics and Rate Oscillations of the Oxidation of Propylene Oxide on Polycrystalline Silver. *J. Catal.* **1982a**, *74*, 266-274.

Stoukides, M.; Vayenas, C. G. Transient and Steady-State Vapor Phase Electrocatalytic Ethylene Epoxidation. Voltage, Electrode Surface Area, and Temperature Effects. In *Catalysis under Transient Conditions*; ACS Symposium Series 178; American Chemical Society: Washington, DC, 1982b; pp 181-208.

Stoukides, M.; Vayenas, C. G. Solid Electrolyte-Aided Study of Propylene Oxidation on Polycrystalline Silver. *J. Catal.* **1983**, *82*, 45-55.

Subbarao, E. C.; Maiti, H. S. Solid Electrolytes with Oxygen Ion Conduction. *Solid State Ionics* **1984**, *11*(4), 317-338.

Suzuki, K.; Mori, K. Rate of Desorption of CO from Liquid Iron. *Trans. ISIJ* **1977**, *17*, 136-142.

Teague, C. E. The High Temperature Ammonia Fuel Cell: Production of Nitric Oxide with Cogeneration of Electricity. M.Sc. Thesis, Massachusetts Institute of Technology, Cambridge, 1981.

Takeda, Y.; Kanno, R.; Noda, M.; Tomida, Y.; Yamamoto, O. Cathodic Polarization Phenomena of Perovskite Oxide Electrodes with Stabilized Zirconia. *J. Electrochem. Soc.* **1987**, *134*(11), 2656-2661.

Vayenas, C. G. Comment on "Interpretation of the Electromotive Forces of Solid Electrolyte Concentration Cells during CO Oxidation on Platinum and on Electromotive Force Studies of CO Oxidation on Platinum". *J. Catal.* **1984**, *90*, 371-373.

Vayenas, C. G. Catalytic and Electrocatalytic Reactions in Solid Oxide Fuel Cells. *Solid State Ionics* **1988**, *28-30*, 1521-1539.

Vayenas, C. G.; Farr, R. D. Cogeneration of Electric Energy and Nitric Oxide. *Science* **1980**, *208*, 593-594.

Vayenas, C. G.; Lee, B.; Michaels, J. N. Kinetics, Limit Cycles, and Mechanism of the Ethylene Oxidation on Platinum *J. Catal.* **1980**, *66*, 36-48.

Vayenas, C. G.; Debenedetti, P. G.; Yentekakis, I.; Hegedus, L. L. Cross-Flow, Solid-State Electrochemical Reactors: A Steady-State Analysis. *Ind. Eng. Chem. Fundam.* **1985**, *24*, 316-324.

Vayenas, C. G.; Bebelis, S.; Neophytides, S. Non-Faradaic Electrochemical Modification to Catalytic Activity. *J. Phys. Chem.* **1988**, *92*, 5083-5085.

Wagner, C. Adsorbed Atomic Species as Intermediates in Heterogeneous Catalysis. *Adv. Catal.* **1970**, *21*, 323-381.

Weissbart, J.; Ruka, R. A Solid Electrolyte Fuel Cell. *J. Electrochem. Soc.* **1962**, *109*(8), 723-726.

Winkler, O.; Bakish, R. *Vacuum Metallurgy*; Elsevier: Amsterdam, 1971.

Yentekakis, I. V.; Vayenas, C. G. The Effect of Electrochemical Oxygen Pumping on the Steady-State and Oscillatory Behavior of CO Oxidation on Polycrystalline Pt. *J. Catal.* **1988**, *111*, 170-187.

Yentekakis, I. V.; Vayenas, C. G. Chemical Cogeneration in Solid Electrolyte Cells: The Oxidation of H_2S to SO_2. *J. Electrochem. Soc.* **1989**, *136*, 996-1002.

Yentekakis, I. V.; Neophytides, S.; Vayenas, C. G. Solid Electrolyte Aided Study of the Mechanism of CO Oxidation on Polycrystalline Platinum. *J. Catal.* **1988**, *111*, 152-169.

Received for review September 23, 1988
Revised manuscript received May 30, 1989
Accepted June 13, 1989

Common Mass Spectrometric Characteristics of Durable Press Reactants Based on Cyclic Ureas

Brenda J. Trask-Morrell,* Bethlehem A. Kottes Andrews, and William E. Franklin
Southern Regional Research Center, Mid South Area, Agricultural Research Service, USDA, New Orleans, Louisiana 70179

Solid probe mass spectrometric analyses were performed on 16 compounds based on cyclic ethyleneurea or cyclic propyleneurea. These compounds are used in durable press finishing of cotton textiles. The mass spectral ion profiles were examined to reveal common characteristics that are related to compound structure. Possible fragmentation routes were suggested to account for the majority of ions produced by these agents. The *N*-methylol-substituted agents are ones that easily release formaldehyde, which is a problem for the textile industry. The mass spectral technique provided a new means of identifying such agents and may find applications in the textile industry as a means of monitoring the ability of etherifying agents to suppress formaldehyde release of finishing agents.

Durable press (DP) reactants used in the textile finishing industry are often based on derivatives of cyclic ureas. Ethyleneurea (EU) and propyleneurea (PU) are the structural skeletons upon which many agents are built. The ones most commercially successful in the past were adducts of cyclic ureas and formaldehyde, that is, methylol derivatives of the cyclic ureas. We recently began research to achieve a basic understanding of the thermal stability of these reactants (Trask-Morrell and Kottes Andrews, 1988). By use of thermal analyses, a variety of common structural characteristics were recognized. The most important finding was a means to identify some agents capable of releasing formaldehyde.

A number of these same cyclic compounds were examined by solid probe mass spectrometric (MS) analyses. With this technique, we were able to support our thermal marker for formaldehyde release with a mass spectrometric marker (Trask-Morrell et al., 1987, 1988). Some concurrent research has been reported on a group of durable press agents in the GC/mass spectrometer (Beck et al., 1988).

The research reported here is a presentation of the results of MS solid probe analyses of 16 compounds based on ethylene- and propyleneureas. The aim is to elucidate some features common to these compounds through mass spectrometric analyses.

Materials and Methods

The reagents analyzed were urea, unsubstituted cyclic ethyleneurea, and propyleneurea, as well as compounds that contained groups symmetrically substituted, unless stated otherwise. Substituents on the ring nitrogens included CH_2OH, CH_3, and CH_2OCH_3. Substituents on the